The International Journal of Advanced Manufacturing Technology (2023) 127:1559–1573
https://doi.org/10.1007/s00170-023-11537-4

ORIGINAL ARTICLE

Investigation on electrochemical characteristics of forged Ti-48Al-2Cr-2Nb in $NaNO_3$ solution for its application on the manufacture of aero-engine blades

Yudi Wang[1] · **Zhengyang Xu**[1]

Received: 10 November 2022 / Accepted: 4 May 2023 / Published online: 30 May 2023

Abstract
Electrochemical machining (ECM) has great advantages for the manufacture of difficult-to-cut γ-TiAl alloys considering its many inherent advantages over traditional cutting techniques. In this study, the ECM characteristics of a new forged Ti-48Al-2Cr-2Nb (TiAl 4822) intermetallic with α and γ phases were investigated in $NaNO_3$ solution. The polarization characteristics of the sample were studied by potentiodynamic and potentiostatic polarization tests. The results show that the alloy has typical active, passive, and transpassive regions, and the compactness and corrosion resistance of passive film are getting better and better with the increase of test time at passive potential. The XPS test revealed that the main components of the passive film are titanium dioxide and aluminum oxide. Furthermore, the alloy exhibits high material removal rates that remain almost constant in the range of current density less than 50 A/cm^2. Moreover, the dissolution mechanism of TiAl 4822 alloy was also revealed through the dissolution morphology, elemental composition, surface roughness, and intergranular corrosion at different current densities. The sample shows a loose lamellar dissolution morphology and is very rough at low current density. The sample exhibits a very flat surface at high current density, but many micro-bulges with high content of Cr element on the dissolved surface. Finally, several forged TiAl 4822 alloy blades were successfully fabricated with an average surface roughness of Ra 0.55 μm. It proves that ECM can obtain high surface quality and high material removal rate of forged TiAl 4822 alloy for complex structural components in aero-engines.

Keywords Electrochemical machining · Ti-48Al-2Cr-2Nb · Electrochemical dissolution characteristic · Polarization behavior · Blade

1 Introduction

To meet the increasingly high-performance requirements of aero-engines, such as lighter weight, less nitride emissions and noise, new materials are urgently needed. Gamma titanium aluminum (γ-TiAl) alloy can meet these challenges due to its many advantages, such as low density, high specific strength, and superior mechanical properties. Among the above advantages, the most noteworthy is that the density of γ-TiAl alloy is only about 4.0 g/cm^3, which is half lighter than nickel-based superalloy and has become the frontrunner to replace nickel-based superalloy components in aero-engines [1, 2]. However, γ-TiAl alloys also exhibit some disadvantages, including low thermal conductivity and low room temperature ductility. It is not easy to process γ-TiAl alloy into complex structure parts (such as blades) by traditional cutting methods (such as milling, grinding, or turning), which often cause micro-cracks, lamellae deformation, working hardening layer, or even fracture defects [3–6]. Some untraditional processing methods are also used to process such alloys. For electrical discharge machining and laser machining, recasting layers, micro-cracks, or residual stresses are usually formed on the surface of samples, which have serious adverse effects on the serve life of parts [7, 8]. Electron beam melting and addictive manufacturing usually result in very rough surface and poor profile accuracy [9, 10]. ECM is a very economical and promising manufacturing method for γ-TiAl alloy, which can overcome the above shortcomings.

✉ Zhengyang Xu
xuzhy@nuaa.edu.cn

[1] College of Mechanical and Electrical Engineering, Nanjing University of Aeronautics and Astronautics, 29 Yudao Street, Nanjing 210016, People's Republic of China

ECM is a non-contact cold processing method, which mainly removes metal materials according to electrochemical anodic dissolution principle and is controlled by Faraday's law. ECM has many advantages such as no loss of tool electrode, no residual stress and recasting layer, high machining efficiency, good surface quality, and processing difficult-to-cut materials independent of their physical properties [11–13]. After many years of development, ECM has been considered as one of the indispensable manufacturing methods for the key parts of aero-engine [14]. It has successfully manufactured titanium alloy and nickel-based superalloy blade or blisk [15–18], stainless steel and nickel-based superalloy casing [19, 20], large size TiAl 45XD alloy blade [21], etc.

The outstanding mechanical properties of γ-TiAl intermetallic and the inherent advantages of ECM technology attracted many scholars to carry out scientific research on the ECM of γ-TiAl intermetallic, and has made considerable progress. Liu et al. conducted a series of ECM experiments for cuboid Ti-46Al-4Nb-2(Cr, Ta) (at.%) intermetallic specimens with an area size of 15×10 mm^2 and surface roughness of the workpiece up to Ra 1 μm using optimized parameters [22]. Weinmann et al. reported the ECM properties of Ti90Al6V4 and Ti60Al40 alloys in different solutions using a series of electrochemical testing techniques. The results show that titanium content has a certain inhibitory effect on electrochemical dissolution of the sample [23]. Clifton et al. reported that processed γ-TiAl alloy (Ti-45Al-2Mn-2Nb (at.%) 0.8 vol.% TiB_2) specimens usually have high surface integrity without significant structural defects for the ECM process, but the surface hardness of the specimens is 46% lower than that of the turning process [24]. Klocke and Wang proved that γ-TiAl alloy in $NaNO_3$ solution has better surface quality compared to NaCl solution [25, 26]. Wang et al. studied the passive properties of two typical γ-TiAl intermetallic compounds and found that the surface passive film structure mainly consists of a dense inner film and a loose outer film [27]. The above research results have great guiding significance for the content of this paper. Generally speaking, different kinds of materials or materials formed by different process methods usually have different ECM characteristics [28]. Forged Ti-48Al-2Cr-2Nb alloy is a promising second-generation intermetallic compound. However, there are few reports on ECM of forged TiAl 4822 intermetallic.

In this paper, the ECM characteristics of forged TiAl 4822 alloy in $NaNO_3$ solution were studied, and the corresponding blades were successfully manufactured. First, the phase composition and microstructure of forged TiAl 4822 alloy were observed by X-ray diffractometer (XRD) and metallographic microscope. Second, the electrochemical polarization behavior of forged TiAl 4822 alloy was revealed by potentiostatic and potentiodynamic polarization. At the same time, the composition of the passive film formed on the surface of the sample at passive potential (1 V) was also determined by X-ray photoelectron spectroscopy (XPS) technology, which will show that the main components of the passive film are titanium dioxide and aluminum oxide. Third, the material removal rate of forged TiAl 4822 alloy at 1–50 A/cm^2 was measured by weighing method. Moreover, the dissolved morphology, surface roughness, elemental composition, and intergranular corrosion of forged TiAl 4822 alloy at various current densities were analyzed by field emission scanning electron microscopy (FESEM), surface roughness instrument, energy dispersive X-ray spectroscopy (EDS), and metallographic microscope. The electrochemical dissolution schematic models of forged TiAl 4822 alloy were also established. Finally, the ECM experiments of forged TiAl 4822 alloy blade were carried out. The specific ECM fixture and tool electrode were designed for the blade. At the same time, the machining phenomenon and surface roughness of forged TiAl 4822 alloy blades after machining were described.

2 Experimental processes

2.1 Sample preparation

Forged TiAl 4822 alloy was used as an anode material for electrochemical tests and ECM experiments, and its main elements were obtained using EDS (X-flash 5010; Bruker, Germany), as shown in Fig. 1. It can be seen that the alloy contains a large amount of Ti and Al elements. Moreover, the addition of Nb can increase its oxidation resistance and creep resistance, as well as high temperature strength. A small amount of Cr can improve its ductility [1]. The sample's size for electrochemical testing and dissolution morphology analysis is $10 \times 10 \times 10$ mm^3, and its surface was grinded by wet sandpaper with different mesh numbers before the test.

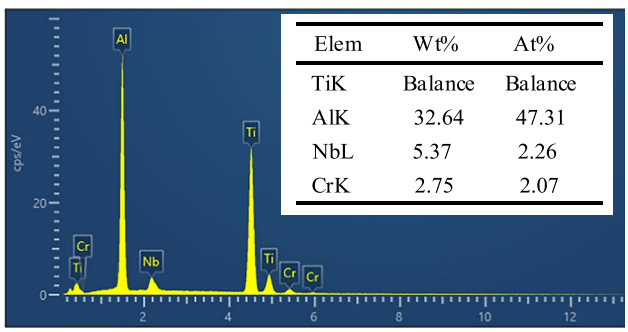

Elem	Wt%	At%
TiK	Balance	Balance
AlK	32.64	47.31
NbL	5.37	2.26
CrK	2.75	2.07

Fig. 1 EDS of forged TiAl 4822 alloy

2.2 Anode polarization behavior

Polarization behavior is a very important part in the analysis of anodic electrochemical dissolution characteristics. In this study, the polarization behavior of forged TiAl 4822 alloy was mainly tested by electrochemical workstation (Zennium E; Zahner Instruments Inc., Germany) and electrolytic cell. The schematic diagram of the test system is shown in Fig. 2. The test system is mainly composed of electrochemical workstation, electrolytic cell, thermostatic water cycle equipment, and computer, which belongs to a three-electrode test system. The workpiece is a forged TiAl 4822 alloy and only the surface (1 cm^2) parallel to the platinum electrode was not covered with insulation. The saturated calomel electrode was used as the reference electrode and the platinum electrode with higher purity was used as the counter electrode. For the electrolytic cell, it mainly consists of two layers. The inner layer is mainly $NaNO_3$ solution, and the outer layer is mainly circulating water.

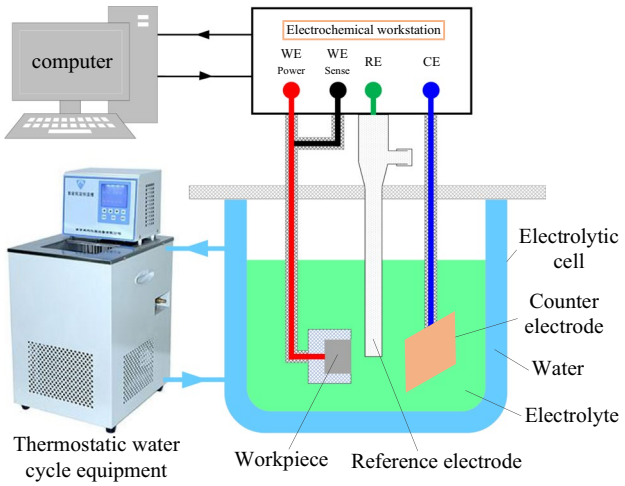

Fig. 2 Schematic diagram of polarization behavior measuring device

The surface passive film was measured by XPS (AXIS Supra; Kratos, Japan) technique after potentiostatic polarization to determine its composition. A monochromatic Al Kα radiation source was used with a measurement area of $300 \times 700\ \mu m^2$. The high-resolution spectra of several main elements in forged TiAl 4822 alloy matrix were detected, and the C 1 s peak at 284.8 eV was used to calibrate binding energy values.

2.3 ECM experiments

The material removal rate, dissolution morphology, surface roughness, and intergranular corrosion of samples are also very important research contents in the analysis of electrochemical dissolution properties. In order to carry out a series of subsequent ECM experiments, a set of ECM equipment system was designed (see Fig. 3), which mainly includes machine tool, electrolyte circulating filtration device, and specific fixture. The ECM equipment mainly consists of a vertical axis and two horizontal axes, which can realize the vertical and horizontal direction of movement. The movement of all motion axes is precisely regulated by numerical control system. In this study, it is necessary to mention that the vertical axis is mainly used for material removal rate testing and dissolution experiments under different current densities, while the two horizontal axes are mainly used for ECM experiments of aero-engine blades. The function of electrolyte circulation filtration system is mainly to transport a continuous flow of $NaNO_3$ solution for processing

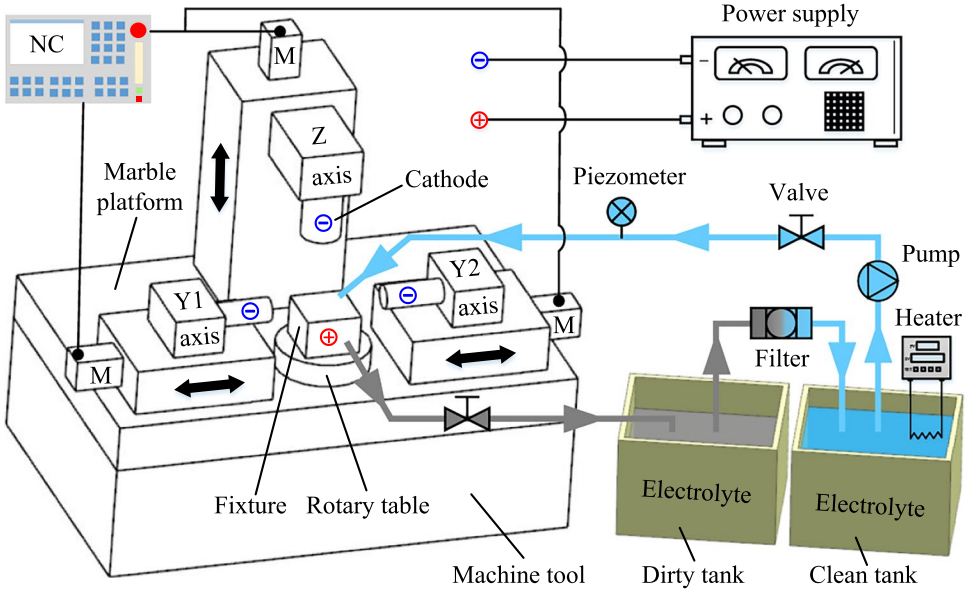

Fig. 3 Schematic diagram of ECM equipment system

and to filter the dirty $NaNO_3$ solution to ensure the stability of processing.

The dissolved morphology, elemental composition, surface roughness, and intergranular corrosion of the samples were analyzed by FESEM (S4800; Hitachi, Japan), EDS, surface roughness instrument (Perthometer M300C; Mahr GmbHs, Germany), and metallographic microscope (Zeiss Axioplan 2 Imaging and Axiophot 2 microscope) after ECM experiments. In addition, the surface quality and morphology of forged TiAl 4822 alloy blade were measured and observed.

3 Results and discussion

3.1 Material analysis

ECM mainly removes metal materials in the form of ionic state. The electrochemical dissolution properties and the surface quality of components are greatly influenced by the microstructure of workpiece [25, 26, 28]. Therefore, the phase composition and microstructure morphology of forged TiAl 4822 alloy matrix were first detected and observed in this study to better analyze some phenomena in ECM, as shown in Fig. 4. It can be seen from the XRD patterns in Fig. 4a that the forged TiAl 4822 alloy mainly contains γ-TiAl and α_2-Ti_3Al phases. Figure 4b exhibits the metallographic morphology of forged TiAl 4822 alloy, which shows a typical duplex structure. Careful observation shows that the forged TiAl 4822 alloy primarily consists of many fine γ-TiAl grains and coarse lamellar colonies arranged alternatively with γ-TiAl and α_2-Ti_3Al phases. Furthermore, it can also be seen that there are obvious differences in the orientation of the lamellae in many lamellar colonies, resulting in dissimilar microscopic morphology due to different perspectives.

3.2 Polarization behavior

3.2.1 Potentiodynamic polarization

The polarization curves of sample in four concentrations of $NaNO_3$ solution (0.1%, 1%, 10%, and 20%) were obtained to explore the effect of electrolyte concentration on the electrochemical polarization behavior of forged TiAl 4822 alloy (see Fig. 5a). In the test, the scanning rate is 10 mV/s, and the voltage is measured from − 2 V to + 4 V. Figure 5a shows that in the transpassive region of the polarization curve, the current density is very small when the electrolyte concentration is 0.1% or 1%. In particular, for 0.1% $NaNO_3$ solution, the current density is only 0.0106 A/cm^2 at the end of the scan. There is only a little corrosion, indicating that the

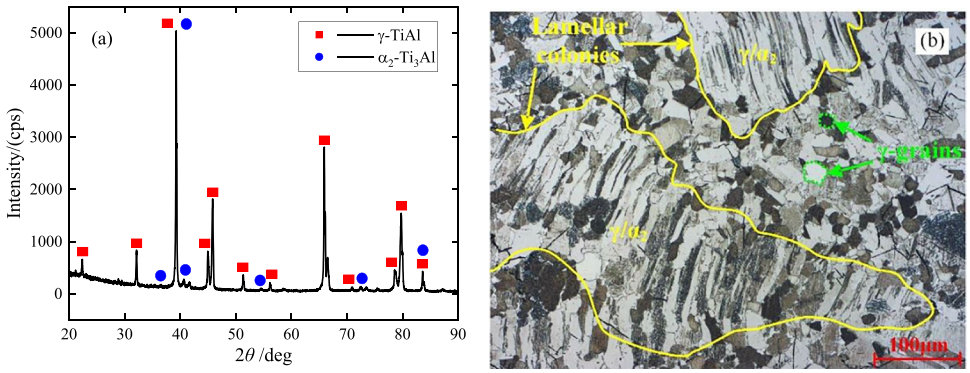

Fig. 4 Phase composition and metallographic morphology of forged TiAl 4822 alloy: **a** XRD pattern and **b** metallographic morphology

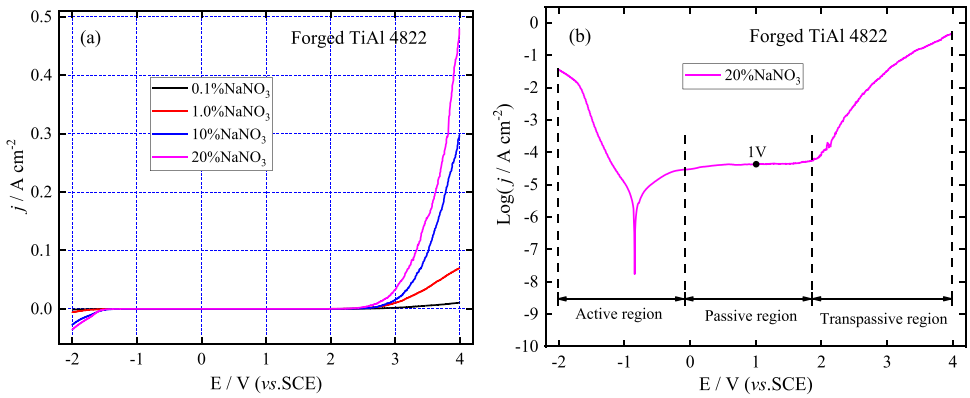

Fig. 5 Polarization curves of forged TiAl 4822 alloy at 30 °C: **a** different concentrations and **b** 20% $NaNO_3$

dissolution rate of forged TiAl 4822 alloy is very low in the low concentration of $NaNO_3$ solution. As the electrolyte concentration increases to 10%, the current density of the polarization curve increases obviously. When the electrolyte concentration is 20%, the polarization curve becomes very steep and the current density increases further. This is because the higher the concentration of electrolyte, the higher the conductivity and the faster the exchange rate of reactive ions [26]. This means that forged TiAl 4822 alloy has a faster reactive ion exchange rate in 20% $NaNO_3$ solution compared to other concentrations. In addition, a careful observation of the transition zone between passive region and transpassive region in Fig. 5a shows that forged TiAl 4822 alloy exhibits the lowest breakdown potential in 20% $NaNO_3$ solution. Based on the above test results, 20%$NaNO_3$ solution was selected to carry out a series of subsequent experiments in this study, considering its higher material removal and lower breakdown potential. Figure 5b shows the polarization curve of forged TiAl 4822 alloy with semi-logarithm, which exhibits typical active–passive–transpassive transition behavior. Interestingly, the current density is small and remains about constant in the passive region, indicating the presence of a passive film. The current density increases rapidly when the machining enters the transpassive region. This is mainly due to the increasing scanning voltage forcing the passive film to crack and be removed, resulting in electrochemical dissolution of the forged TiAl 4822 alloy.

Figure 6a shows the cyclic voltammetry (CV) curve of forged TiAl 4822 alloy, which is a positive hysteresis loop throughout the scanning process. In the forward scan (-2 V $\rightarrow +4$ V), the curve almost increased linearly with the increase of the scanning voltage in the transpassive region, which shows Ohmic behavior and that the resistance of the $NaNO_3$ solution is dominant [29]. In the reverse scan ($+4$ V $\rightarrow -2$ V), the current density of the alloy decreases gradually with the decrease of scanning voltage. When the reverse scanning voltage is reduced to 1.64 V, the sample enters passive state again, and its current density is almost zero. Interestingly, the current density in reverse scanning process is always higher than that in forward scanning process under similar scanning voltage, which indicates that the surface state of forged TiAl 4822 alloy has changed, that is, it may be subject to uneven corrosion [27, 30]. The polarization morphology of the sample after CV was also observed (see Fig. 6b). There is clearly some localized corrosion occurring on the sample surface, which also verifies the above analysis of CV curve.

3.2.2 Potentiostatic polarization

It can be seen from the above analysis that there will be a passive film at passive potential for forged TiAl 4822 alloy. To further understand the formation process and composition of passive film, potentiostatic polarization test and XPS analysis were carried out. Figure 7 shows the potentiostatic curve of TiAl 4822 alloy at passive potential (1 V) for 1 h. The curve decreases rapidly at the initial stage and then slightly as the test time increases due to the gradual growth of the passive film at passive potential. Figure 7b shows the double-logarithmic plot of current density–time of forged TiAl 4822 alloy. The current density in the figure can be expressed in time as

$$j = 10^{-(b+klogt)} \tag{1}$$

where j is the current density; b and k are constants; t is the time of the test. In particular, k is the slope of the curve in Fig. 7b. The larger the absolute value of k, the denser and more corrosion resistant the passive film [31].

It can be observed from Fig. 7b that the curve becomes steeper and steeper with the increase of test time, indicating that the passive film becomes more and more dense and corrosion resistant during the growth process. A careful observation of the curve in the figure shows that it mainly consists of three stages and can be fitted with three straight lines with different slopes. At the initial stage, the curve is very gentle, with a slope of about -0.13 for the fitting line. This is mainly related to the loose passive film in the initial phase. In the intermediate stage, the slope of the fitting line is about -0.48, and the compactness of the passive film

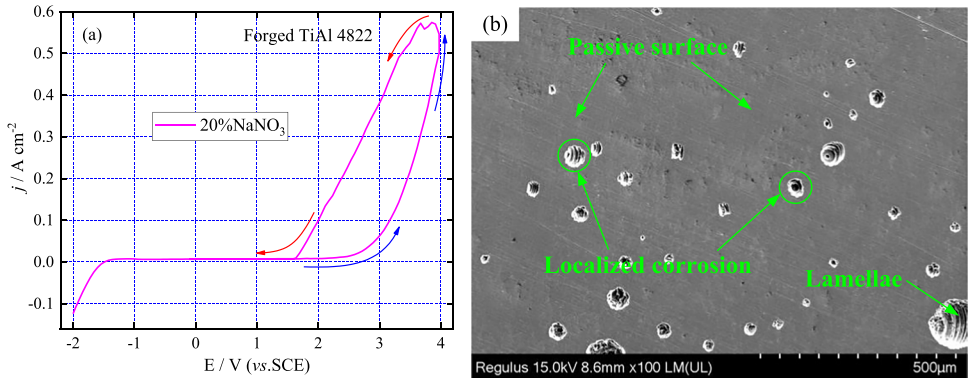

Fig. 6 CV curve and polarization surface of forged TiAl 4822 alloy at 30°: **a** CV curve (50 mV/s) and **b** polarization morphology

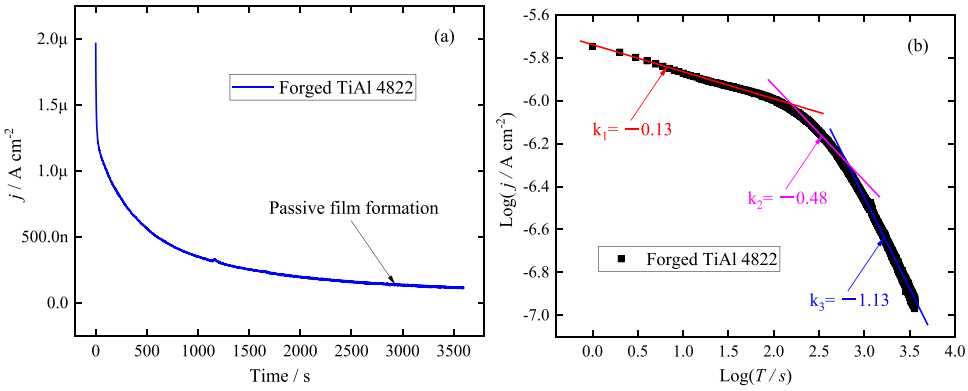

Fig. 7 The potentiostatic polarization curve of forged TiAl 4822 alloy at 1 V for 1 h: **a** current density–time curve and **b** double-logarithmic plot of current density–time

is further enhanced. In the final stage, the curve becomes very steep, with a slope of about − 1.13 for the fitting line. This means that the passive film is very dense and corrosion resistant.

After potentiostatic polarization, the composition of passive film of forged TiAl 4822 alloy was solved by XPS technology. The high-resolution spectrogram mainly detects the main elements Ti and Al in the matrix material based on the EDS results in Fig. 1, as well as O elements in the passive film. The test data were processed and fitted by commercial software CasaXPS.

Figure 8a shows that the XPS spectra of Ti 2p mainly consists of four components, and the binding energies are 458.32 and 464.04 eV, 453.12 and 459.53 eV corresponding to TiO_2 2p3/2 and TiO_2 2p1/2, metal Ti 2p3/2 and Ti 2p1/2 spin–orbit doublets, respectively. Figure 8b shows that the XPS spectrum of Al 2p can be fitted by two components at the binding energies of 71.51 and 73.91 eV, which correspond to Al_2O_3 2p and metal Al 2p, respectively. The peaks of metals titanium and aluminum were also detected in the passive film. This may be because the passive film is porous. The above analysis results show that the passive film primarily consists of TiO_2 and Al_2O_3, which are oxides of metal elements Ti and Al. Meanwhile, the XPS spectrum of O 1 s in the passive film was also analyzed. It can be found that it is mainly composed of two peaks, corresponding to TiO_2 and Al_2O_3 at the position of 529.82 and 531.56 eV, respectively. It is further confirmed that the passive film is primarily consist of TiO_2 and Al_2O_3. The good corrosion resistance of forged TiAl 4822 alloy is closely related to Al_2O_3 in the passive film.

3.3 Material removal rate

In this study, the weighting method was used to determine the material removal rates of forged TiAl 4822 alloy under various current densities [26]. The experiment was repeated twice to ensure the accuracy of the test. Figure 9 shows the relationship between material removal rate ($\eta\omega$) and current density (j) for forged TiAl 4822 alloy. It is clear from the figure that forged TiAl 4822 alloy dissolves at low current density and exhibits a higher material removal rate compared to other high current densities. And then, the material removal rate of the alloy hardly changes within the current density range tested. Figure 9 also shows that the results of the two experiments are almost identical, indicating a very good repeatability. In general, forged TiAl 4822 alloy exhibits a very high $\eta\omega$ compared to normal titanium alloy and nickel-based superalloy in $NaNO_3$ (or NaCl) solution

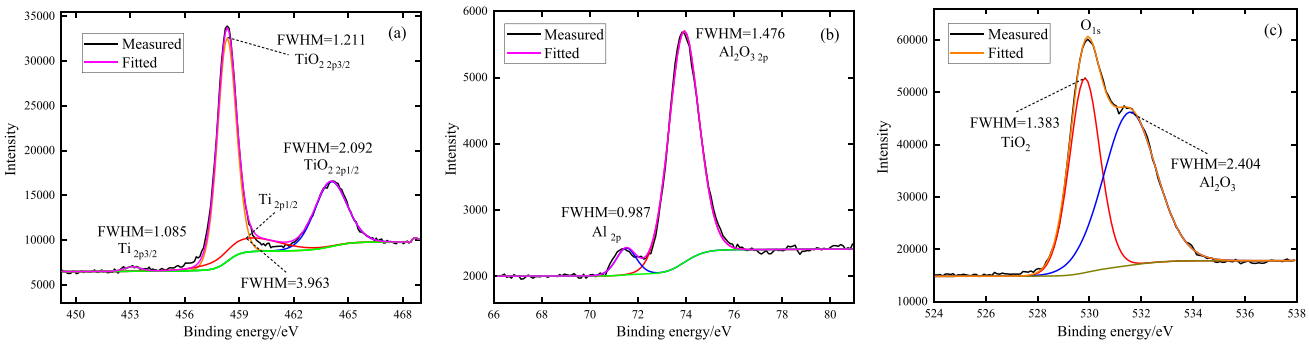

Fig. 8 High-resolution XPS spectra of Ti, Al, and O elements for passive film on the surface of forged TiAl 4822 alloy

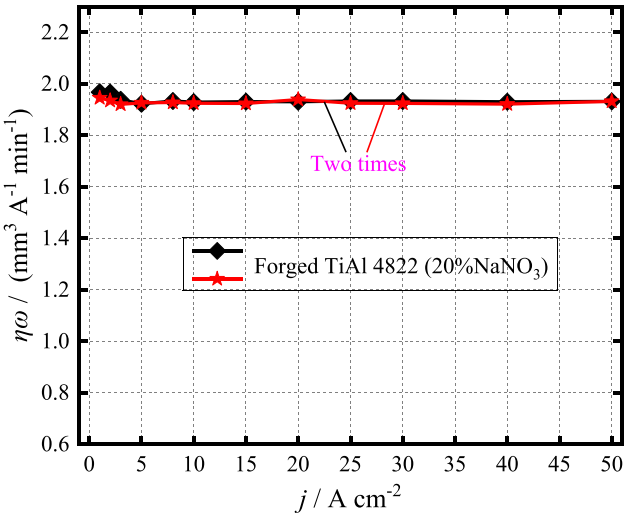

Fig. 9 $\eta\omega$–j curve of forged TiAl 4822 alloy in $NaNO_3$ solution at 30 °C

[5, 28]. It also reflects that the high efficiency machining of forged TiAl 4822 alloy can be realized by ECM.

3.4 Dissolution experiments at various current densities

Electrochemical dissolution experiments under various current densities were conducted to further understand the ECM characteristics and anode dissolution mechanism of forged TiAl 4822 alloy. The surface dissolution morphology, processing quality, elemental composition, and intergranular corrosion for the samples were measured in detail after dissolution experiment. The size of the sample used in the experiment is $10\times10\times10$ mm^3, and the inlet pressure of the electrolyte is about 0.1 MPa.

4 Dissolution morphology analysis

The dissolved morphologies of forged TiAl 4822 alloy at 1, 5, 20, and 50 A/cm^2 are shown in Fig. 10. In processing, the sample's surface passes similar amounts of electricity ($Q=It$). It can be seen from these figures that the forged TiAl 4822 alloy exhibits different dissolved morphologies under different current densities. In Fig. 10a, the forged TiAl 4822 alloy has serious non-uniform electrochemical dissolution and coarse lamellar colonies were exposed, showing a very loose lamellar dissolution morphology. In addition, it is worth mentioning that these loose lamellae may flake off in a non-ECM due to uneven dissolution and the scouring effects of the high-speed flowing electrolyte. This appears to be the reason why forged TiAl 4822 alloy exhibits slightly higher $\eta\omega$ values at 1, 2, or 3 A/cm^2. At 5 A/cm^2, forged TiAl 4822 alloy still presents a loose and uneven lamellar dissolution morphology, but the exposed lamellar size decreases slightly. At 20 A/cm^2, the dissolved surface of forged TiAl 4822 alloy is greatly improved, and the loose lamellar substances almost disappear. It is worth noting that there are many micro-protrusions and exposed lamellar colonies for forged TiAl 4822 alloy. At 50 A/cm^2, the machined surface becomes very flat. However, there are still many micro-bulges and exposed lamellar colonies. A closer inspection reveals that the height of these micro-bulges and the exposed lamellar colonies is significantly reduced. This is mainly related to the more uniform dissolution of the material at 50 A/cm^2. Moreover, it also reflects that the electrochemical removal rates of γ and α phases in the lamellar colony are different based on the exposed lamellar colony.

In order to further reveal the micro-bulges on the dissolved surface of forged TiAl 4822 alloy, the chemical composition and EDS mapping of raised and non-raised areas in Fig. 10d were obtained. Figure 11 shows that there is no difference in the element content between the labeled area "a" and the base material of forged TiAl 4822, while the raised area contains higher content of Cr element. By analyzing the standard electrode potential of the main metal elements in forged TiAl 4822 alloy (see Table 1), one possible reason is that Cr element has a relatively high standard electrode potential, which is more difficult to dissolve in ECM. Klocke et al. also reported that Cr element has an adverse effect on the material removal rate of γ -TiAl alloy due to its affinity in passive or oxide layers formation [5]. Figure 12 shows EDS mapping of main metal elements and C and O elements in Fig. 10. From these figures, it can be seen more clearly that the distribution of Cr element in the raised region on the dissolved surface is lighter to other regions, indicating that the content of Cr element in the raised region is relatively high. It is further proved that Cr content is high in the micro-bulge under high current density.

5 Surface roughness analysis

The surface quality of the sample was also measured at four current densities. In order to make the results more accurate and reliable, the ECM experiments under different current densities were repeated twice. Moreover, six measuring lines were uniformly selected from the machined surface for surface roughness measurement. Figure 13a shows the schematic diagram of measurement line selection. The relationship between average surface roughness and current density of forged TiAl 4822 alloy is shown in Fig. 13b. It can be seen that the two experimental measurements almost coincide, indicating good repeatability. In general, the surface roughness value of forged TiAl 4822 alloy decreases significantly

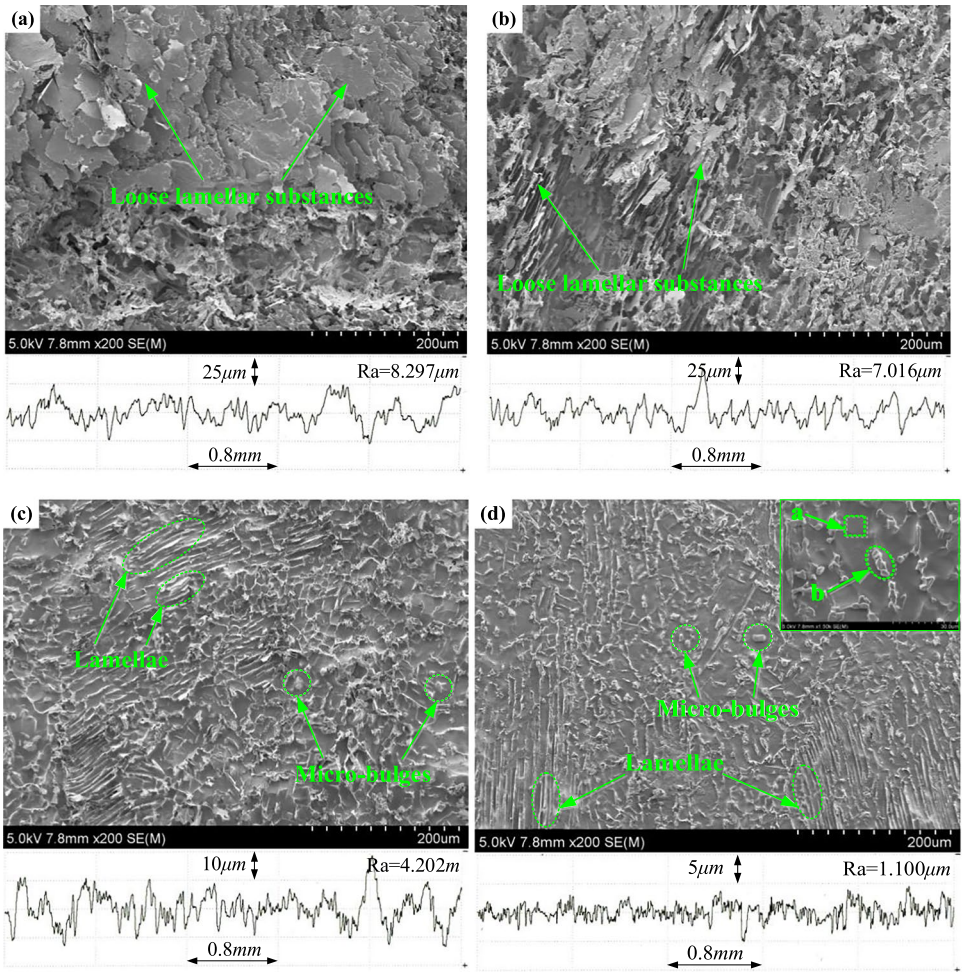

Fig. 10 Surface morphologies of forged TiAl 4822 at different current densities: **a** 1 A/cm^2 for 1000 s, **b** 5 A/cm^2 for 200 s, **c** 20 A/cm^2 for 50 s, and **d** 50 A/cm^2 for 20 s

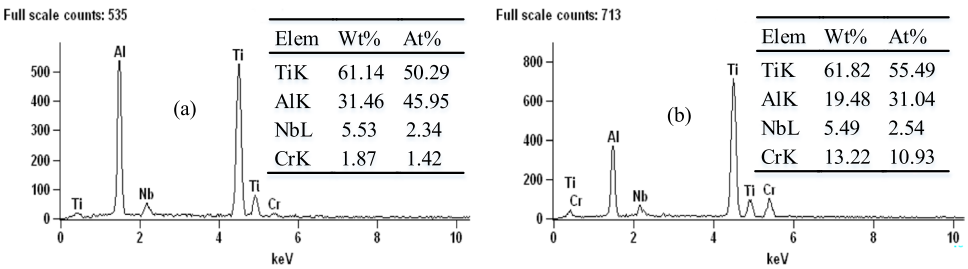

Fig. 11 EDS of forged TiAl 4822 marked area in Fig. 10d: (a) area "a" and area "b"

Table 1 Standard electrode potential of main elements in specimens

Anodic chemical reaction	Standard electrode potential (V)
$Al \rightarrow Al^{3+} + 3e$	− 1.66
$Ti \rightarrow Ti^{2+} + 2e$	− 1.63
$Nb \rightarrow Nb^{3+} + 3e$	− 1.1
$Cr \rightarrow Cr^{3+} + 3e$	− 0.74

with the increases of current density. Figure 13b reveals that the Ra value of the sample exceeds 7 when the current density is very low (1 or 5 A/cm^2), suggesting that the machining quality is bad. This is mainly due to the uneven dissolution of materials at 1 or 5 A/cm^2, resulting in the existence of many loose lamellar substances for forged TiAl 4822 according to SEM results. At 20 A/cm^2, the surface quality is greatly improved. This can be

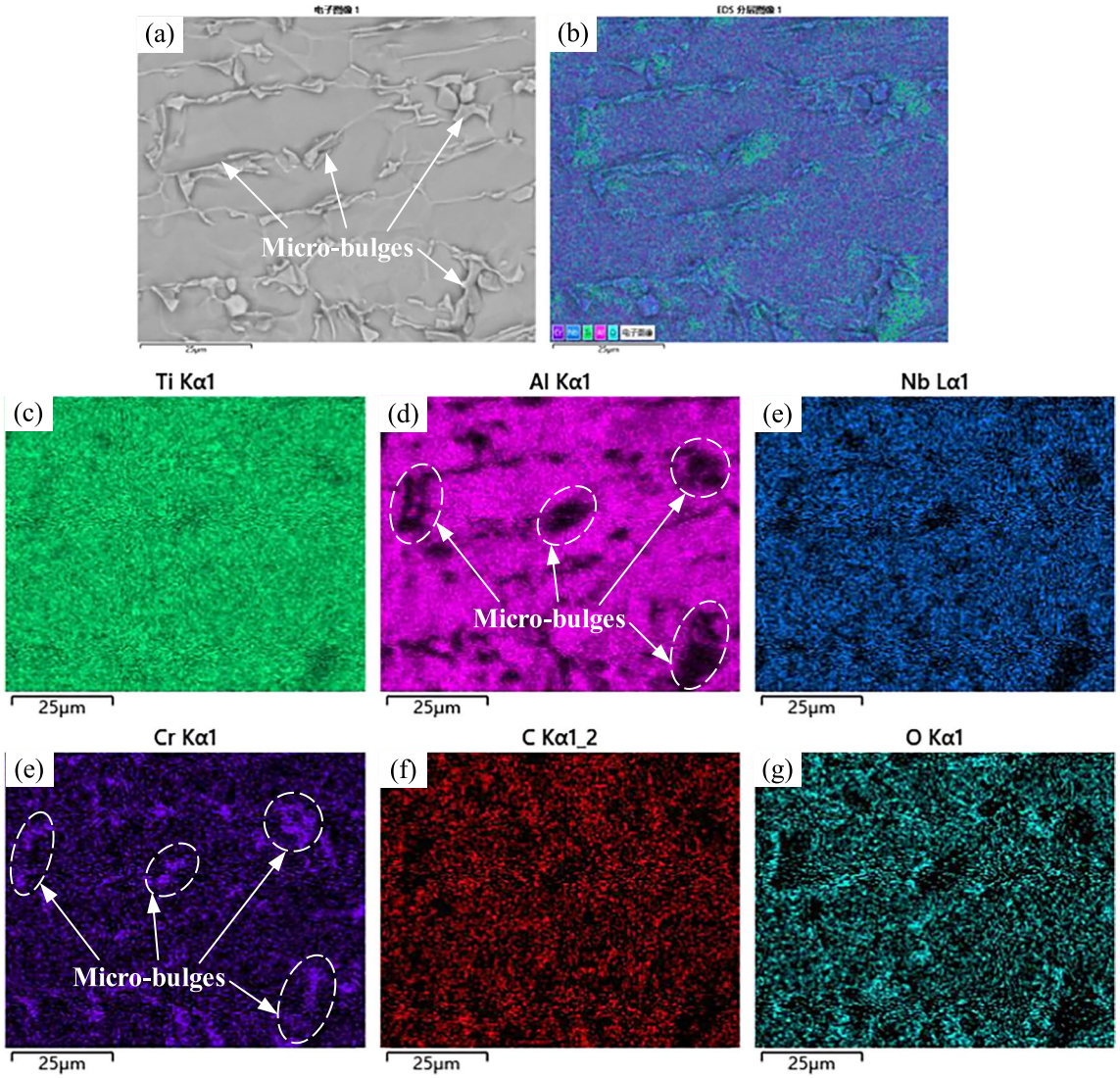

Fig. 12 EDS mapping of high magnification in Fig. 10d

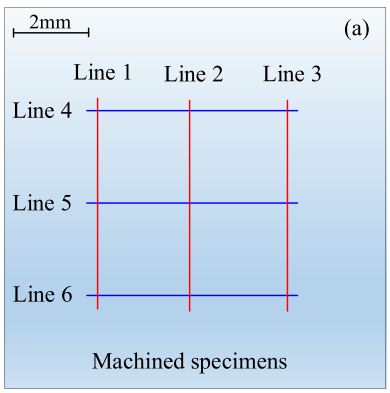

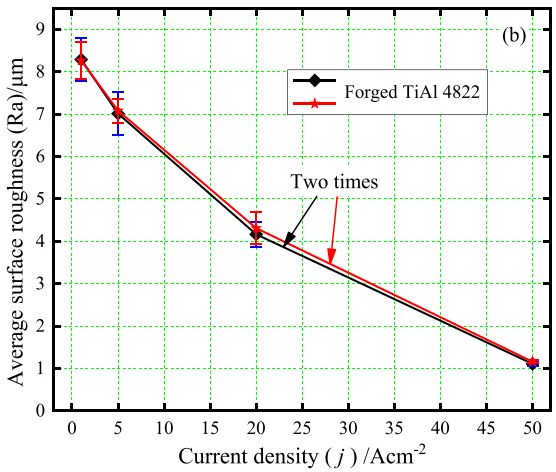

Fig. 13 Surface roughness of forged TiAl 4822 alloy at different current densities: **a** measuring lines, **b** surface roughness

interpreted as the removal of loose lamellar substances (see Fig. 10c). At 50 A/cm^2, the Ra value of forged TiAl 4822 alloy is approximately 1.1 μm. This indicates that ECM really has the potential to achieve good machining quality for forged TiAl 4822 alloy.

6 Intergranular corrosion analysis

Intergranular corrosion will have a great adverse effect on the service life of parts (such as blades). In order to improve the service life of parts and avoid serious accidents, it is necessary to ensure that there are no intergranular corrosion defects on the surface of specimens. Therefore, the intergranular corrosion of forged TiAl 4822 alloy was observed and analyzed in this section. Figure 14a and b show the cross-sections of forged TiAl 4822 alloy at 5 and 50 A/cm^2 after ECM, respectively. These two images and their local magnified images show that there is no intergranular corrosion defect, which is mainly because the alloy is made by forging process and its grains are refined and grain boundaries are improved. Moreover, localized corrosion is observed in Fig. 14a, showing an uneven dissolved morphology. It can also be observed from Fig. 14b and its enlarged image that the machined surface of the sample is very flat, but there are some micro-bulges.

7 Dissolution model building

According to the previous studies, the dissolution models of forged TiAl 4822 alloy in $NaNO_3$ solution were established to better understand the electrochemical dissolution mechanism of the alloy. Based on the polarization behavior test results, the passive film will form for forged TiAl 4822 alloy at passive potential, which has a certain hindering effect on material dissolution. The passive film is primarily contains titanium dioxide and aluminum oxide according to the XPS measurement in Fig. 8. As shown in Fig. 15a, the matrix of the alloy contains many coarse lamellar colonies and refined γ grains based on the XRD pattern and metallographic morphology in Fig. 4. At low current density, the lamellae in the matrix are obvious and the surface is uneven due to non-uniform dissolution, resulting in poor surface quality of the sample (see Fig. 10a and b). In addition, these loose wafers may flake off in a non-ECM manner, resulting in a slightly higher $\eta\omega$ at low current density, according to the results in Figs. 9 and 10. Figure 15b is the dissolution model at high current density. At high current density, the loose wafers are almost completely removed, but there are many micro-bulges (see Fig. 10c and d). The content of Cr in these micro-raised areas is high due to its high standard electrode potential according to the results in Fig. 11, Fig. 12, and Table 1. Importantly, forged TiAl 4822 alloy leaves a smooth dissolution surface at high current density due to more uniform dissolution.

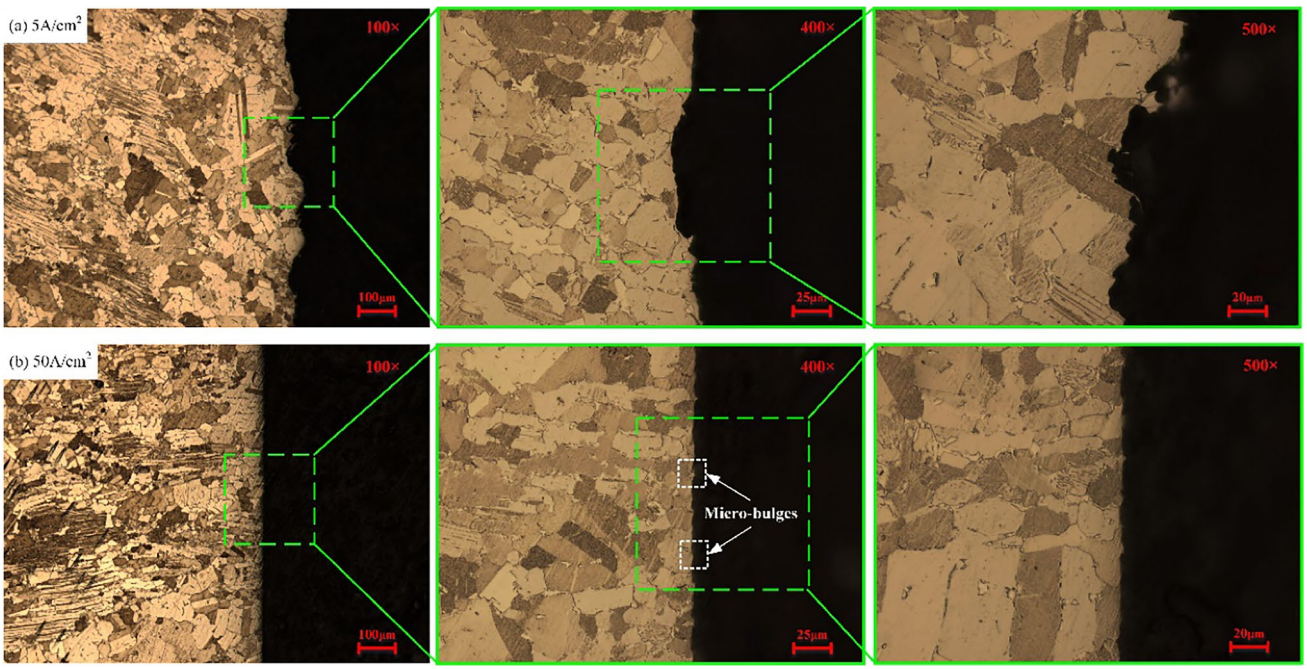

Fig. 14 Cross-sections of forged TiAl 4822 alloy at different current densities: **a** 5 A/cm^2 and **b** 50 A/cm.^{2}

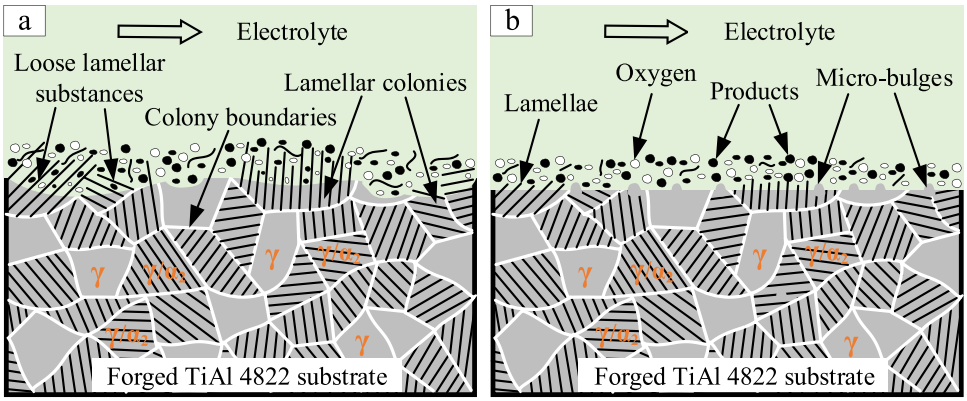

Fig. 15 Dissolution models of forged TiAl 4822 alloy at low and high current densities: **a** low current density and **b** high current density

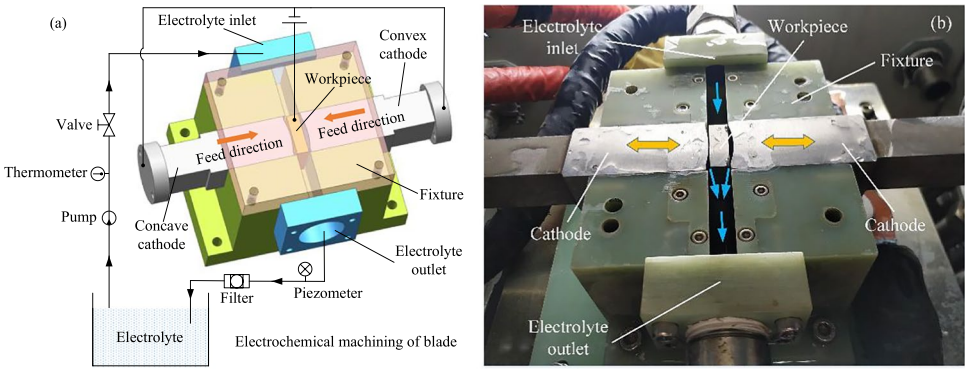

Fig. 16 ECM fixture for forged TiAl 4822 blade: **a** 3D model and **b** physical picture

8 ECM of aero-engine blades

The forged TiAl 4822 alloy's most promising application field is blade parts in aero-engine. The above basic studies prove that ECM can achieve high surface integrity of forged TiAl 4822 alloy at high current density. In this section, therefore, ECM experiments for forged TiAl 4822 alloy blades were carried out based on the machine tool equipment system (see Fig. 3). The machining current, machining quality, and microstructure for the manufactured blades were also analyzed in detail.

8.1 ECM experiments of forged TiAl 4822 blades

Figure 16a and b are the 3D model of the self-designed ECM fixture and the physical picture of the machining area in the machine tool, respectively. The main part of the fixture and the positioning reference of the workpiece are made of insulated fiberglass and rigid stainless steel, respectively. The machining area is located in a closed space in the fixture and has a pre-designed flow channel. The main purpose is to ensure a stable flow of high-pressure electrolyte and fill the entire processing area. Figure 17a and b are the 3D model of standard blade and tool cathodes, respectively. The total processing area of blade concave and blade convex surface is about 17.25 cm^2. The blank of the blade is a cuboid with a size of $49.8 \times 30 \times 10$ mm^3. In the ECM of blade, the blank of forged TiAl 4822 blade and the cathode tool were connected to the positive and negative terminals of the pulse power supply through copper wire, respectively. The high-speed electrolyte flows rapidly through a pre-designed flow channel in the fixture to remove bubbles, Joule heat, and electrolytic sludge. At the same time, the concave cathode and the convex cathode move to the blank of the blade in the opposite direction with the same feed rate. As the cathode tools continue to move, the blank gradually dissolves

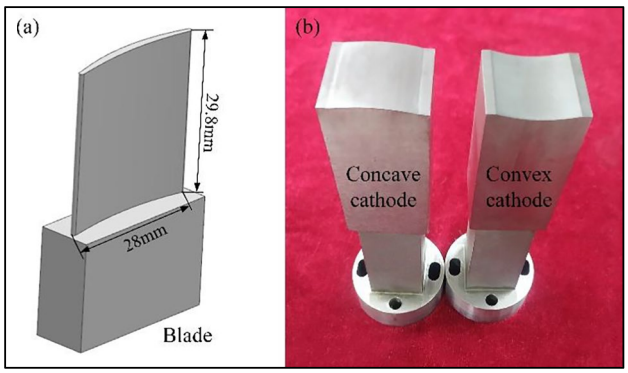

Fig. 17 3D model of standard blade and picture of tool cathodes

Table 2 Experimental parameters

Parameters	Values
Cathode material	Stainless steel
Cathode feeding rate v_c (mm/min)	0.8
Electrolyte concentration	20% $NaNO_3$
Voltage U (V)	22
Pulse frequency (Hz)	100
Pulse duty (%)	50
Inlet pressure P_1 (MPa)	0.6
Outlet pressure P_2 (MPa)	0.1
Electrolyte temperature T (°C)	30 ± 0.5
Initial machining gap δ_0 (mm)	0.5

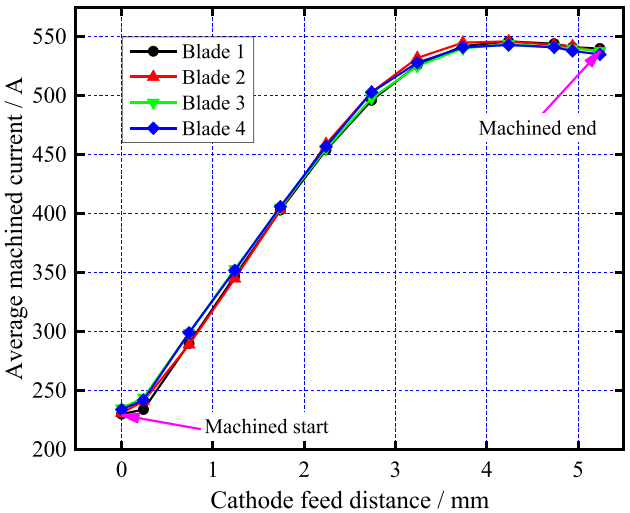

Fig. 18 The relationship between the average machining current of the blades and the cathode feed distance

and eventually forms a shape similar to that of a standard blade. After several pre-experiments, the selected machining parameters for ECM of blades are shown in Table 2.

8.2 Result analysis

Figure 18 shows the relationship between the machining current and the tool electrode feed distance during machining. The curve in the figure can be divided into three stages based on the change of average machining current. The first stage is that the machining current increases rapidly, which is mainly related to the blank gradually dissolving from cuboid shape into standard blade shape. And then, the machining current hardly changes, which is mainly attributed to the forming of the blade and the processing into the equilibrium state. At this stage, the peak current density of the blade is about 63 A/cm^2. In the final stage, the average machining current decreased slightly, which is mainly because the blade leading/trailing edge areas were dissolved, making the machining area decrease slightly. Moreover, the change of the average machining current during process is very smooth without any sudden change. This means that the machining process for the blade is very stable; there is no short circuit phenomenon. It is also obvious that the average current curves of the four blades almost coincide, which means that the machining has very good repeatability.

Figure 19 shows the four blades of forged TiAl 4822 alloy processed by ECM. It can be seen that whether the blade concave or the blade convex, the surface of the blade is very smooth and there is no flow mark and short-circuit burn defects. As shown in Fig. 20, the average surface roughness for the four blades are very similar, about Ra 0.55 μm. The ripple diagram of the surface roughness for the blade is shown in Fig. 21. This further verifies that the experiment has good repeatability. It is interesting that the surface quality of the processed blades is better than that of the basic test samples mentioned above. The main reason is that the processed blades have higher current density and electrolyte pressure, which makes the dissolution of materials more uniform. In addition, the dissolved morphologies of blade concave and blade convex were also photographed through FESEM. Figure 22 shows that the

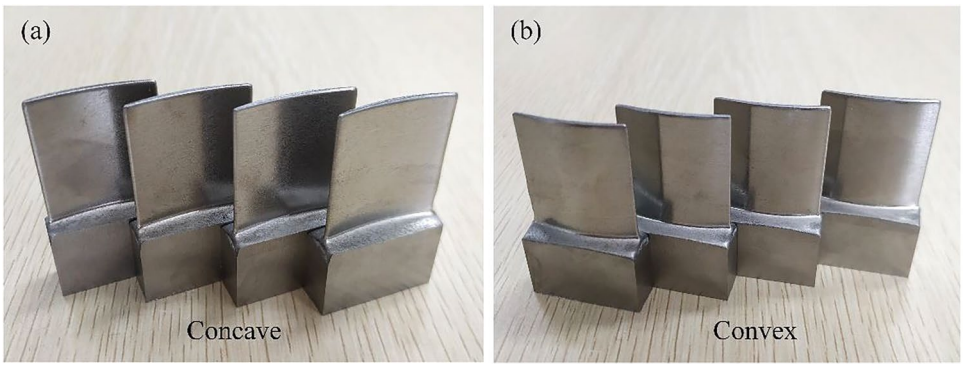

Fig. 19 Machined blades through ECM: **a** blade concave and **b** blade convex

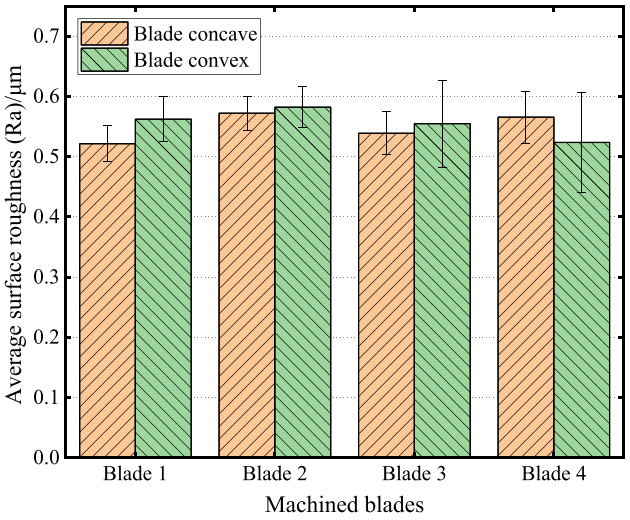

Fig. 20 Surface roughness of machined workpieces

machined morphology is indeed quite smooth, and the height and number of micro-bulges on the dissolved surface are significantly reduced. It also shows that the forged TiAl 4822 alloy can obtain better surface quality by ECM under higher current density and electrolyte pressure.

These results show that current density has an important effect on surface quality of forged TiAl 4822 workpiece. In order to obtain better surface quality, parameters such as cathode feeding rate or machining voltage or duty ratio can be increased within a certain range, and the optimal parameter combination can be optimized to achieve higher current density.

9 Conclusions

In this paper, the polarization characteristics, material removal rate, material removal mechanism at different current densities, and blade manufacturing of forged TiAl 4822 alloy were studied. It is proved that ECM is a potential processing method for forged TiAl 4822 alloy, which can obtain high processing efficiency, high machining quality, and no intergranular corrosion defects of complex structural components. Here are the conclusions:

1. The potentiodynamic polarization test show that forged TiAl 4822 alloy has obvious active, passive, and transpassive regions. There are some localized corro-

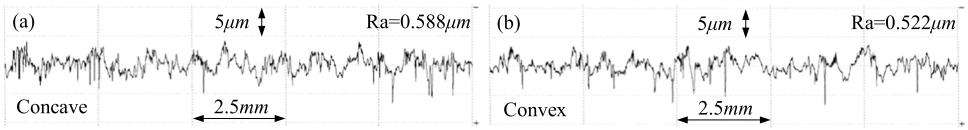

Fig. 21 Ripple diagram of the surface roughness: **a** concave and **b** convex

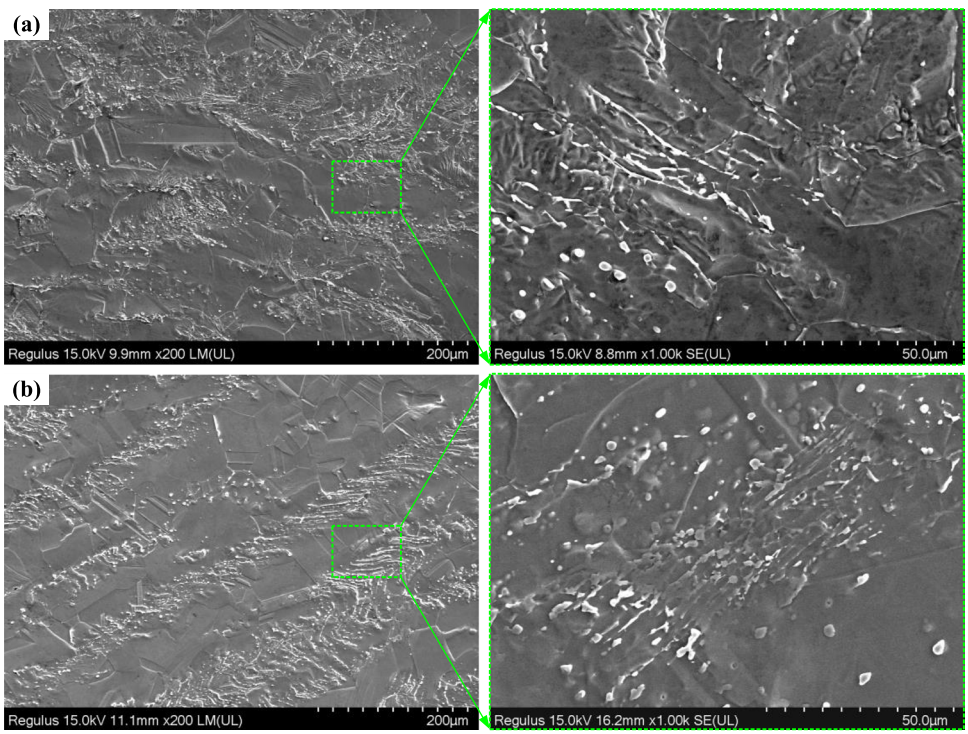

Fig. 22 The dissolved morphologies of blade: **a** blade concave and **b** blade convex

sion in the polarization morphology of sample after CV. The results of potentiostatic polarization test show that the formation process of passive film on forged TiAl 4822 alloy surface can be divided into three stages at passive potential, and the compactness and corrosion resistance of passive film become better and better with the increase of testing time. The passive film primarily consists of titanium dioxide and aluminum oxide according to XPS measurement results.

2. Forged TiAl 4822 alloy dissolves at low current density and exhibits a higher material removal rate compared to other high current densities. Also, the material removal rate of the alloy hardly changes under other high current densities.
3. The lamellae are all exposed at low current density, showing a loose lamellar dissolution morphology due to non-uniform dissolution. The dissolved surface of forged TiAl 4822 alloy is very flat due to more uniform dissolution at high current density. However, many micro-bulges were formed on the dissolved surface. EDS results show that the content of Cr element in these micro-raised areas is higher due to its high standard electrode potential. Moreover, corresponding electrochemical dissolution models were established to characterize the electrochemical dissolution behavior of forged TiAl 4822 alloy.
4. Finally, the forged TiAl 4822 alloy blades were fabricated successfully by ECM. The results show that the average surface roughness of the processed blades is about Ra 0.55 μm, and it has good repeatability.

Author contribution YW: conceptualization, methodology, investigation, data curation, experiment, writing—original draft, funding acquisition. ZX: review and editing, supervision, funding acquisition.

Funding This research was sponsored by the National Natural Science Foundation of China [grant number 91960204], the China Postdoctoral Science Foundation [grant number 2022M721603], and the National Natural Science Foundation of China for Creative Research Groups [grant number 51921003].

Declarations

Conflict of interest The authors declare no competing interests.

References

1. Kothari K, Radhakrishnan R, Wereley NM (2012) Advances in gamma titanium aluminides and their manufacturing techniques. Prog Aerosp Sci 55:1–16. https://doi.org/10.1016/j.paerosci.2012.04.001
2. Bewlay BP, Weimer M, Kelly T, Suzuki A, Subramanian PR (2013) The science, technology, and implementation of TiAl alloys in commercial aircraft engines. MRS Proc 1516:49–58. https://doi.org/10.1557/opl.2013.44
3. Mantle AL, Aspinwall DK (1997) Surface integrity and fatigue life of turned gamma titanium aluminide. J Mater Process Technol 72:413–420. https://doi.org/10.1016/S0924-0136(97)00204-5
4. Hood R, Lechner F, Aspinwall DK, Voice W (2007) Creep feed grinding of gamma titanium aluminide and burn resistant titanium alloys using SiC abrasive. Int J Mach Tools Manuf 47:1486–1492. https://doi.org/10.1016/j.ijmachtools.2006.10.008
5. Klocke F, Herrig T, Zeis M, Klink A (2015) Experimental research on the electrochemical machinability of selected γ-TiAl alloys for the manufacture of future aero engine components. Procedia CIRP 35:50–54. https://doi.org/10.1016/j.procir.2015.08.050
6. Kolahdouz S, Hadi M, Arezoo B, Zamani S (2015) Investigation of surface integrity in high speed milling of gamma titanium aluminide under dry and minimum quantity lubricant conditions. Procedia CIRP 26:367–372. https://doi.org/10.1016/j.procir.2014.08.016
7. Sarkar S, Mitra S, Bhattacharyya B (2006) Parametric optimisation of wire electrical discharge machining of γ titanium aluminide alloy through an artificial neural network model. Int J Adv Manuf Technol 27:501–508. https://doi.org/10.1007/s00170-004-2203-7
8. Biswas R, Kuar AS, Mitra S (2014) Multi-objective optimization of hole characteristics during pulsed Nd:YAG laser microdrilling of gamma-titanium aluminide alloy sheet. Opt Lasers Eng 60:1–11. https://doi.org/10.1016/j.optlaseng.2014.03.014
9. Demirtas H, Yilmaz O, Subasi L, Gunaydin A, Bilgin GM, Orhangul A, Akbulut G, Nesli S (2021) Surface quality improvement using electro chemical machining process for γ-TiAl parts produced by electron beam melting. Procedia CIRP 102:240–245. https://doi.org/10.1016/j.procir.2021.09.041
10. Xu ZF, Ouyang WT, Liu YF, Jiao JK, Liu YZ, Zhang WW (2021) Effects of laser polishing on surface morphology and mechanical properties of additive manufactured TiAl components. J Manuf Process 65:51–59. https://doi.org/10.1016/j.jmapro.2021.03.014
11. Wang YD, Xu ZY, Zhang A, Xu GC, Zhang CX (2021) Surface morphology and electrochemical behaviour of Ti-48Al-2Cr-2Nb alloy in low-concentration salt solution. Sci China Technol Sci 64:283–296. https://doi.org/10.1007/s11431-019-1558-8
12. Xu ZY, Wang YD (2021) Electrochemical machining of complex components of aero-engines: developments, trends, and technological advances. Chinese J Aeronaut 34:28–53. https://doi.org/10.1016/j.cja.2019.09.016
13. Rajurkar KP, Zhu D, McGeough JA, Kozak J, De Silva A (1999) New developments in electro-chemical machining. CIRP Ann - Manuf Technol 48:567–579. https://doi.org/10.1016/S0007-8506(07)63235-1
14. Wang YD, Xu ZY, Liu J, Zhang A, Meng DM, Zhao JB (2021) Study on flow field of electrochemical machining for large size blade. Int J Mech Sci 190:106018. https://doi.org/10.1016/j.ijmecsci.2020.106018
15. Klocke F, Klink A, Veselovac D, Aspinwall DK, Soo SL, Schmidt M, Schilp J, Levy G, Kruth J (2014) Turbomachinery component manufacture by application of electrochemical, electro-physical and photonic processes. CIRP Ann - Manuf Technol 63:703–726. https://doi.org/10.1016/j.cirp.2014.05.004
16. Chen XZ, Xu ZY, Zhu D, Fang ZD, Zhu D (2016) Experimental research on electrochemical machining of titanium alloy Ti60 for a blisk. Chinese J Aeronaut 29:274–282. https://doi.org/10.1016/j.cja.2015.09.010
17. Zhang JC, Zhu D, Xu ZY, Zhang KL, Liu J, Qu NS, Zhu D (2016) Improvement of trailing edge accuracy in blisk electrochemical machining by optimizing the electric field with an extended cathode. J Mater Process Technol 231:301–311. https://doi.org/10.1016/j.jmatprotec.2015.12.025

18. Zhu D, Yu LG, Zhang RH (2018) Dissolution effects with different microstructures of Inconel 718 on surface integrity in electrochemical machining. J Electrochem Soc 165:E872–E878. https://doi.org/10.1149/2.0761816jes
19. Wang DY, Wang QQ, Zhang J, Le HY, Zhu ZW, Zhu D (2021) Counter-rotating electrochemical machining of intensive cylindrical pillar array using an additive manufactured cathode tool. Int J Mech Sci 211:106653. https://doi.org/10.1016/j.ijmecsci.2021.106653
20. Wang DY, Zhu ZW, He B, Zhu D, Fang ZD (2018) Counter-rotating electrochemical machining of a combustor casing part using a frustum cone-like cathode tool. J Manuf Process 35:614–623. https://doi.org/10.1016/j.jmapro.2018.09.016
21. Wang YD, Xu ZY, Meng DM, Liu L, Fang ZD (2022) Study on surface roughness of large size TiAl intermetallic blade in electrochemical machining. J Manuf Process 76:1–10. https://doi.org/10.1016/j.jmapro.2022.01.035
22. Liu J, Zhu D, Zhao L, Xu ZY (2015) Experimental investigation on electrochemical machining of γ-TiAl intermetallic. Procedia CIRP 35:20–24. https://doi.org/10.1016/j.procir.2015.08.049
23. Weinmann M, Stolpe M, Weber O, Busch R, Natter H (2015) Electrochemical dissolution behaviour of Ti90Al6V4 and Ti60Al40 used for ECM applications. J Solid State Electrochem 19:485–495. https://doi.org/10.1007/s10008-014-2621-x
24. Clifton D, Mount AR, Jardine DJ, Roth R (2001) Electrochemical machining of gamma titanium aluminide intermetallics. J Mater Process Technol 108:338–348. https://doi.org/10.1016/S0924-0136(00)00739-1
25. Klocke F, Herrig T, Zeis M, Klink A (2018) Comparison of the electrochemical machinability of electron beam melted and casted gamma titanium aluminide TNB-V5. Proc Inst Mech Eng Part B J Eng Manuf 232:586–592. https://doi.org/10.1177/0954405416687147
26. Wang YD, Xu ZY, Zhang A (2019) Electrochemical dissolution behavior of Ti-45Al-2Mn-2Nb+0.8 vol% TiB_2 XD alloy in NaCl and $NaNO_3$ solutions. Corros Sci 157:357–369. https://doi.org/10.1016/j.corsci.2019.06.010
27. Wang YD, Xu ZY, Zhang A (2020) Anodic characteristics and electrochemical machining of two typical γ-TiAl alloys and its quantitative dissolution model in $NaNO_3$ solution. Electrochim Acta 331:135429. https://doi.org/10.1016/j.electacta.2019.135429
28. Wang XD, Qu NS, Guo PF, Fang XL, Lin X (2017) Electrochemical machining properties of the laser rapid formed Inconel 718 alloy in $NaNO_3$ solution. J Electrochem Soc 164:E548–E559. https://doi.org/10.1149/2.1221714jes
29. Liu WD, Ao SS, Li Y, Liu ZM, Zhang H, Manladan SM, Luo Z, Wang ZP (2017) Effect of anodic behavior on electrochemical machining of TB6 titanium alloy. Electrochim Acta 233:190–200. https://doi.org/10.1016/j.electacta.2017.03.025
30. Ittah R, Amsellem E, Itzhak D (2014) Pitting corrosion evaluation of titanium in NH_4Br solutions by electrochemical methods. Int J Electrochem Sci 9:633–643. https://doi.org/10.1002/9780470976524.ch30
31. Zhang LN, Ojo OA (2020) Corrosion behavior of wire arc additive manufactured Inconel 718 superalloy. J Alloys Compd 829:154455. https://doi.org/10.1016/j.jallcom.2020.154455